The Coefficient of Friction of Chrysotile Gouge at Seismogenic Depths

DIANE E. MOORE,[1] DAVID A. LOCKNER,

U. S. Geological Survey, MS/977, 345 Middlefield Road, Menlo Park, California 94025

HIDEMI TANAKA,

Department of Earth and Planetary Science, University of Tokyo, Hongo 7-3-1, Bunkyo-ku, Tokyo, Japan

AND KENGO IWATA

Department of Geo/Biosphere Sciences, Faculty of Science, Ehime University, Bunkyo-cho 2-5, Matsuyama, Japan

Abstract

We report new strength data for the serpentine mineral chrysotile at effective normal stresses, $\overline{\sigma}_n$ between 40 and 200 MPa in the temperature range 25°–280°C. Overall, the coefficient of friction, μ (= shear stress/effective normal stress) of water-saturated chrysotile gouge increases both with increasing temperature and $\overline{\sigma}_n$, but the rates vary and the temperature-related increases begin at ~100°C. As a result, a frictional strength minimum (μ = 0.1) occurs at low $\overline{\sigma}_n$ at about 100°C. Maximum strength (μ = 0.55) results from a combination of high normal stress and high temperature. The low-strength region is characterized by velocity strengthening and the high-strength region by velocity-weakening behavior. Thoroughly dried chrysotile has μ = 0.7 and is velocity-weakening. The frictional properties of chrysotile can be explained by its tendency to adsorb large amounts of water that acts as a lubricant during shear. The water is progressively driven off the fiber surfaces with increasing temperature and pressure, causing chrysotile to approach its dry strength. Depth profiles for a chrysotile-lined fault constructed from these data would pass through a strength minimum at ~3 km depth, where sliding should be stable. Below that depth, strength increases rapidly as does the tendency for unstable (seismic) slip. Such a trend would not have been predicted from the room-temperature data. These results therefore illustrate the potential hazards of extrapolating room-temperature friction data to predict fault zone behavior at depth. This depth profile for chrysotile is consistent with the pattern of slip on the Hayward fault, which creeps aseismically at shallow depths but which may be locked below 5 km depth.

Introduction

OF THE THREE common serpentine minerals—lizardite, antigorite, and chrysotile—chrysotile is the most distinctive crystallographically. Lizardite has the platy form characteristic of sheet-silicate minerals, whereas antigorite adopts a corrugated variation of the platy structure. In chrysotile, however, the layers are rolled up into hollow tubes averaging 110 Å inner diameter and 260 Å outer diameter (Deer et al., 1962). The tubes form with the octahedral ("brucite") sheet on the outside, exposing $(OH)^-$ ions on their outer surfaces; this causes chrysotile to have a high surface potential in water and gives it a marked hydrophilic character (Hodgson, 1966).

The frictional behavior of chrysotile also differs from that of lizardite and antigorite. The room-temperature coefficient of friction, μ, of chrysotile is only about half that of the other two serpentine minerals (Moore et al., 1997; see also Reinen et al., 1994, whose "lizardite" samples are in fact chrysotile, as reported by Reinen and Tullis, 1995). In addition, whereas the strengths of lizardite and antigorite increase modestly with increasing temperature, μ of chrysotile more than doubles with heating to ~280°C (Moore et al., 1997), which is near its upper thermal limit of stability in natural occurrences (e.g., Coleman, 1971; O'Hanley et al., 1989).

Nearly all of the experiments in our earlier investigations of chrysotile strength in the temperature range 25–280°C (Moore et al., 1996b, 1997) were run at a single effective normal stress, $\overline{\sigma}_n$ of 100 MPa. Although the coefficient of friction for most

[1]Corresponding author; e-mail: dmoore@usgs.gov

TABLE 1. Composition of Chrysotile
Used in This Study

SiO_2	42.77
TiO_2	0.01
Al_2O_3	0.34
Cr_2O_3	0.05
FeO*	3.28
NiO	0.01
MgO	39.92
MnO	0.05
CaO	0.02
Total	86.45
Si	2.01
Al^{IV}	–
Al^{VI}	0.02
Ti	–
Cr	–
Fe^{2+}*	0.13
Ni	–
Mg	2.81
Mn	0.01
Ca	–
O anhydrous	7

*Total Fe as FeO.

minerals varies only slightly with changing $\overline{\sigma}_n$, the strong influence of temperature on chrysotile strength suggested the possibility that normal stress might also be an important factor. The purpose of this study was to expand our data set for chrysotile to a wider range of effective normal stresses, and to explore the effects of water on its strength, in order to improve our understanding of this mineral's behavior at depth in fault zones.

Experiments Conducted

Chrysotile starting material

The chrysotile gouge that we used in our experiments was prepared from a soft, pale greyish green rock specimen from New Idria, California that was provided by R. G. Coleman. The sample contained only trace amounts of non-serpentine minerals, and the X-ray diffraction pattern indicated the sole presence of clinochrysotile. Chrysotile typically does not depart substantially from the end-member serpentine composition, $Mg_3Si_2O_5(OH)_4$, and microprobe analysis of the starting material (Table 1) indicates only about 5% substitution of Fe and Al for Mg. Because of the purity of the rock specimen, sample preparation consisted merely of hand-grinding the specimen and passing it through an 88 μm diameter sieve to produce a simulated gouge. The chrysotile has the short-fiber form that is typical for chrysotile from the New Idria serpentinite (Mumpton and Thompson, 1975). Individual fibers are on the order of 5 μm in length (Fig. 1).

Procedures

The experimental apparatus used for high-temperature strength tests is illustrated in Figure 2. For the strength experiments, a 1 mm thick layer of gouge was placed along a 30° sawcut in a cylinder 19.1 mm in diameter and 41.3 mm long of antigoritic serpentinite from New Idria, California. A borehole for pore-fluid entry was drilled all the way through the upper half of each cylinder, to ensure that the gouge did not become isolated from the pore fluid system. The borehole was packed with silica beads, which allowed free flow of fluid but minimized the extrusion of gouge into the borehole. The sawcut surfaces were roughened with #60 SiC prior to sample assembly to insure good shear-traction coupling between the driving blocks and the gouge layer.

With the exception of one room-temperature test (Table 2), the samples were placed in annealed copper jackets during the experiments to separate them from the confining-pressure medium (Fig. 2). Reported strengths were corrected for the strength of the jacket at a given temperature; details of the correction procedure are presented by Moore et al. (1996a). Confining pressure was applied first to the sample, followed by pore pressure, using deionized water for the pore fluid. Confining pressure was measured to within 0.02 MPa, at an accuracy of ±0.3 MPa. Pore pressure was measured to a precision of 0.02 MPa and ±0.2 MPa accuracy. The temperature was raised after the pressures had equilibrated; temperature was monitored by a thermocouple inserted along the pore pressure inlet. The samples were positioned in the furnace using insulating pieces of appropriate lengths, such that the temperature maximum was located near one end, with temperature decreasing by 2% across the length of the sample.
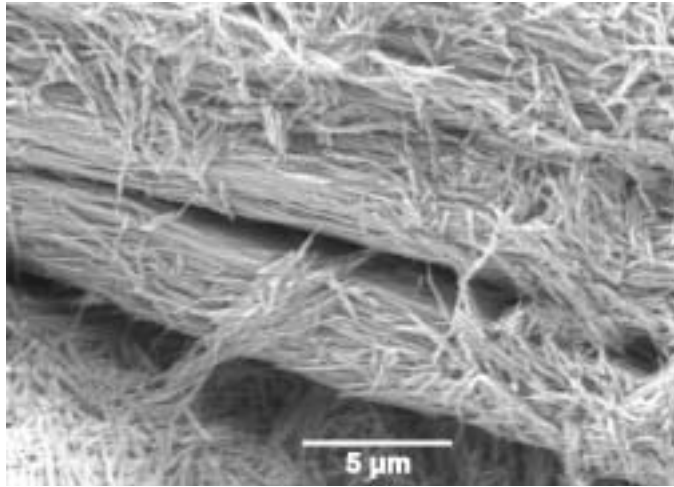
FIG. 1. Backscattered-electron SEM (scanning electron microscope) image of chrysotile gouge starting material, 5000× magnification, showing the short-fiber morphology typical of chrysotile from New Idria (e.g., Mumpton and Thompson, 1975). The hand-grinding procedure did not completely disaggregate the sample, and some clumps of fibers remain.

The space between the copper-jacketed sample and the surrounding resistance heater was loosely packed with boron nitride, which has high thermal conductivity.

The experiments were run at a constant normal stress, which was maintained by means of computer-controlled adjustments to the confining pressure. Axial stress was measured to a precision of 0.1 MPa and an accuracy of 1.0–1.5 MPa, and displacement measurements were made to a precision of 0.1 μm and an accuracy of approximately 5.0 μm. Corrections were made for changes in contact area along the sliding surface, and the absolute value of the seal friction was zeroed out before the start of each experiment. Because seal friction is a function of confining pressure, an additional correction was applied during each experiment to account for the continuing adjustments to confining pressure to maintain a constant normal stress. As a test of pore-fluid communication during the heated experiments, pore pressure was dropped from 30 to 20 MPa during one 281°C experiment (#16 in Table 2) and then returned to 30 MPa after 0.15 mm displacement. The drop in pore pressure was accompanied by an immediate rise in the axial stress, followed by a decrease in confining pressure to maintain constant normal stress. The rapid change in shear strength in response to a change in pore pressure indicates that the gouge layer was in good hydraulic communication with the external pore-pressure system. Except for experiment #1 in Table 2, which was run at a single velocity, the axial short-ening rate was changed at intervals during the experiments to measure the velocity dependence of chrysotile frictional strength (see Figs. 3 and 4). Combining all sources of error, a reported value of frictional strength is estimated to be accurate to within 10%. The reported changes in friction accompanying changes in velocity (Table 2) will be more accurate, because the measurements were made within the same experiment.

We conducted experiments (Table 2) at effective normal stresses of 40, 70, 100, 150, and 200 MPa, at the same temperatures we tested previously (Moore et al., 1996b, 1997). Various combinations of normal stress and pore pressure were used, including one experiment in which the sample was dried overnight in a vacuum oven at 180°C, and then the material was run dry at 97°C. Following the experiments, the samples were cut out of their jackets for examination with a stereomicroscope and a scanning electron microscope (SEM).

Results

Friction experiments

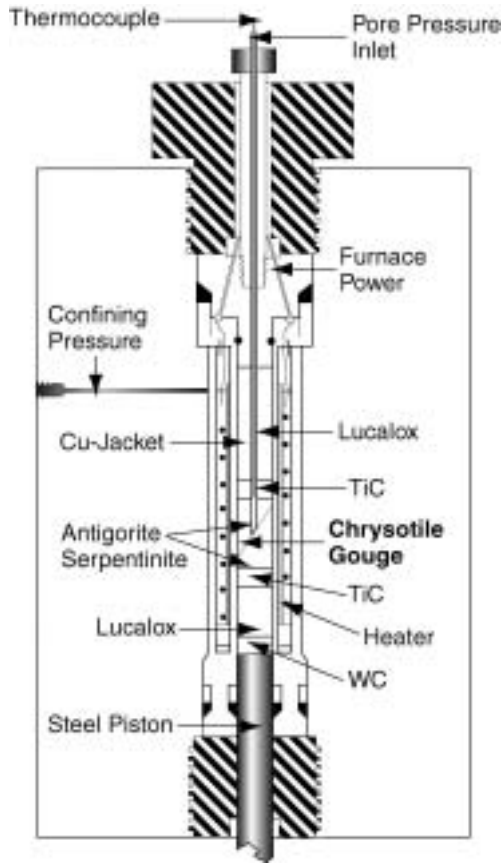The changes in μ with increasing displacement are plotted for all 16 experiments (Table 2) in

FIG. 2. Apparatus used for friction experiments at elevated temperatures.

Figures 3 and 4. The oven-dried sample (Fig. 3A) is the strongest, with μ > 0.7 when the gouge began to slide unstably. This high strength is consistent with that of another oven-dried sample tested by Moore et al. (1997) at room temperature and 100 MPa normal stress; in that experiment, μ had exceeded 0.6 and was still increasing when the dry portion of the experiment was terminated at 1.5 mm axial displacement. Compared to the dry chrysotile sample, the addition of water to only 1 MPa pressure causes a roughly fivefold reduction in μ at 97°C (Fig. 3A). Further increasing the fluid pressure to 100 MPa at the same effective normal stress did not affect the strength. Similarly, increasing pore-fluid pressure from 10 to 100 MPa at constant 100 MPa effective normal stress had no effect on strength at 281°C (Fig. 4B). Thus, the effective stress law [shear stress,

$\tau = \mu(\overline{\sigma_n}) = \mu(\overline{\sigma_n} - Pp)$, where Pp is pore-fluid pressure] holds for water-saturated chrysotile gouge.

For a given effective normal stress, μ was not found to be a monotonic function of temperature. At 200 MPa (Fig. 3C), experiments at 25° and 97°C have nearly identical values of μ. At 40 MPa (Fig. 3B), the 25°C sample is slightly stronger than the 194°C sample over the measured displacement. If only the heated experiments are considered, μ increases with increasing temperature at a given effective normal stress in all cases (Figs. 3B, 3C, and 4). At the same temperature, μ increases with increasing $\overline{\sigma_n}$ for every water-saturated chrysotile sample. At 194°C, for example, μ at 200 MPa (Fig. 3C) is twice that at 40 MPa (Fig. 3B). Several of the experiments in Figures 3 and 4 are characterized by continuous strain hardening, that is most

TABLE 2. Experimental Conditions and Velocity-Step Data

Exp.	σ_n, MPa	T (°C)	σ_n, MPa	Pp, MPa	$\Delta\mu_{ss}$ / ΔlnV		
					logV = –0.5[4]	LogV = –1[5]	logV = –1.5[6]
1[1]	40	25	50	10	–		–
2	40	194	110	70	+0.0025		–0.0050
3	40	281	230	190	–0.0047		–0.0046
4[2]	70	97	70	0	–0.0056		–0.0002
5	70	97	71	1	+0.0044		+0.0026
6	70	97	170	100	+0.0051		+0.0059
7	70	194	80	10	–0.0001 –0.0004	–0.0013	–0.0107
8	70	281	80	10		–0.0061	–0.0057
9	100	281	110	10	–0.0027	–0.0060	–0.0093
10	100	281	200	100	–0.0076	–0.0066	–0.0059
11	150	97	200	50	+0.0067	–0.0069	+0.0047
12	150	194	200	50		–0.0062	–0.0067
13	200	25	210	10	–0.0046		+0.0020
14	200	97	210	10	+0.0022		+0.0015
15	200	194	220	20	–0.0054		–0.0111
16[3]	200	281	230	30	–0.0087		–0.0088

[1]Single velocity, 1 μm/s, to 3.5 mm displacement; sample tested in a polyurethane jacket.
[2]Oven-dried at 180°C; sample run dry.
[3]Pore pressure was lowered to 20 MPa between 2.30 and 2.45 mm displacement (see Fig. 1C).
[4]1.0–0.1 μm/s velocity step.
[5]1.0-0.01 μm/s step.
[6]0.1–0.01 μm/s step.

pronounced at the highest temperatures and lowest velocities tested.

The sliding-rate sensitivity of shear strength is represented by the change in steady-state coefficient of friction, $\Delta\mu_{ss}$, resulting from a logarithmic change in velocity: $\Delta\mu_{ss}$/ΔlnV. The net change in μ with changing velocity is the product of two competing, time-dependent effects, $\Delta\mu_{ss}$/ΔlnV = (a – b), where a is the immediate response to the velocity step, and b is the amount of subsequent decay to the steady-state value of μ (e.g., Rice and Gu, 1983; Logan and Rauenzahn, 1987). Frictional stability of the sliding surface can be evaluated by examining the sign of $\Delta\mu_{ss}$/ΔlnV. Positive values correspond to velocity-strengthening behavior, such that shear remains stable as the sliding speed increases. Nega-

tive values of $\Delta\mu_{ss}$/ΔlnV reflect velocity-weakening behavior where slip potentially may be unstable. The determinations of $\Delta\mu_{ss}$/ΔlnV for these experiments, presented in Table 2, include corrections for seal friction characteristics including absolute values, pressure dependence, and velocity dependence. All but two of the positive values, indicating velocity-strengthening behavior, are from experiments conducted at 97°C.

Gouge textures

The deformation textures developed in the chrysotile samples from this study (Fig. 5) are consistent with those reported previously by Moore et al. (1997) for serpentine-mineral gouges, although the newer-model SEM used in this study allows for
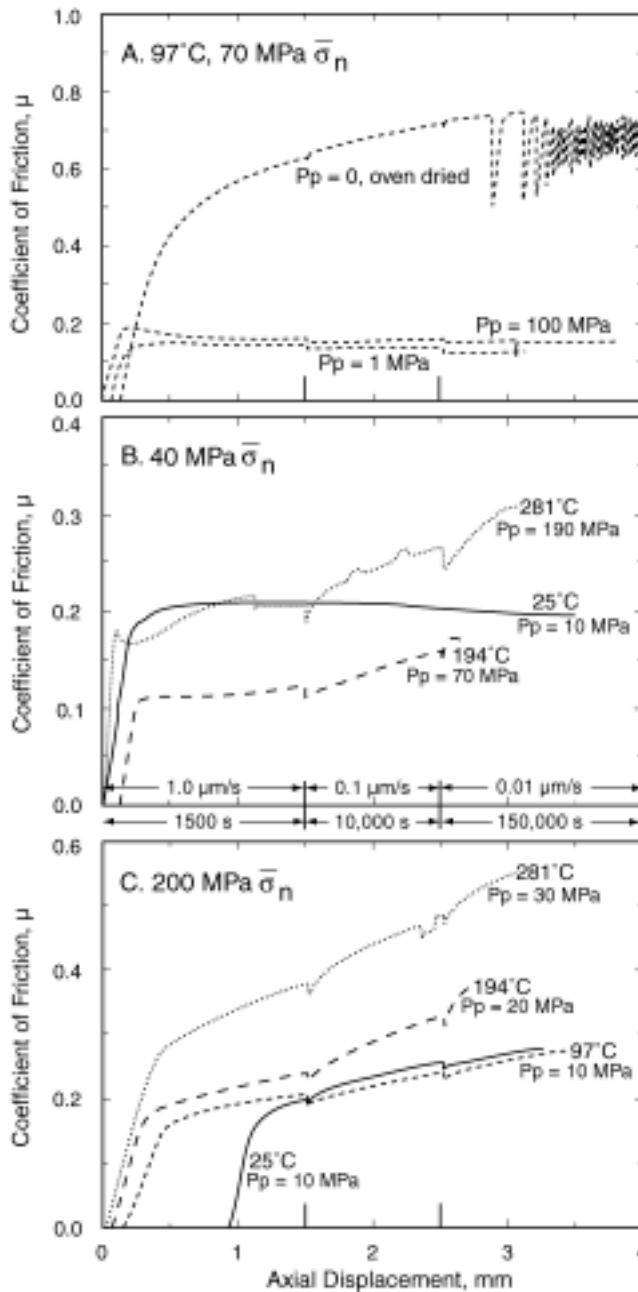
FIG. 3. Friction experiments at: A. 70 MPa $\overline{\sigma}_n$ and 97°C, comparing oven-dried with water-saturated samples at different pore pressures. B. 40 MPa $\overline{\sigma}_n$. C. 200 MPa $\overline{\sigma}_n$. Three velocities were tested in all experiments except for the 25°C run in B. The corrections for Cu-jacket strength were applied after the experiments were completed, which tends to shift the curves somewhat to the right of the origin. The ram was incorrectly zeroed for the 25°C experiment in C, causing the curve to be displaced far to the right. The different line patterns used for the strength plots of Figures 3 and 4 indicate the temperature of the experiment (see Fig. 6A). Axial dislacement, or the rate of advance of the ram (Fig. 2), is plotted in Figures 3 and 4; shear displacement along the sawcut surface would be about 15% larger.
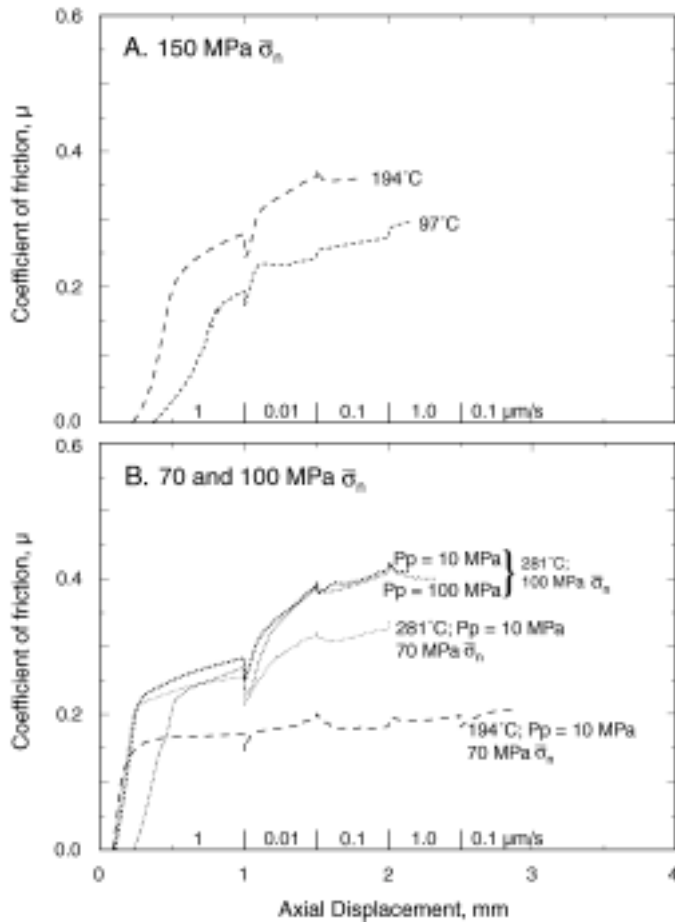
F IG . 4. Friction experiments are: A. 150 MPa $\overline{\sigma}_n$. B. 70–100 MPa $\overline{\sigma}_n$. These experiments were run at a different sequence of velocities from those in Figure 3.

observations at considerably higher magnifications than were possible before. When removed from their jackets, the samples separated along slickensided shear surfaces (Fig. 5A). The most prominent shears are the "boundary" shears that form parallel and close to (but not directly on) the sawcut surfaces of the antigorite forcing blocks. Shear occurs completely within the gouge layer. Numerous Riedel shears cross the gouge layer at relatively small angles (5–24°; Moore et al., 1997) from one boundary shear to the other. The surfaces of the shears have a wavy, or corrugated, appearance (Fig. 5A). Higher magnifications (Figs. 5B and C) reveal the strong preferred alignment of the chrysotile fibers in the shear plane parallel to the direction of shear. The chrysotile fibers are closely

packed on the shear surface (Fig. 5C), but some pores (black in the SEM image) are visible. The terminations of the chrysotile tubes are stubby, and the average fiber length appears to be shorter than in the starting material (Fig. 1).

Shear is highly localized along the narrow boundary and Riedel shears, and the gouge located even a short distance away from the shear surface has a much more randomly oriented and less closely packed texture (Fig. 5D). Such localization of shear and variation in porosity structure are typical of all phyllosilicate-rich gouges (Zhang et al., 2001; Moore and Lockner, 2004). No obvious differences related to changing temperatures and stresses were identified.
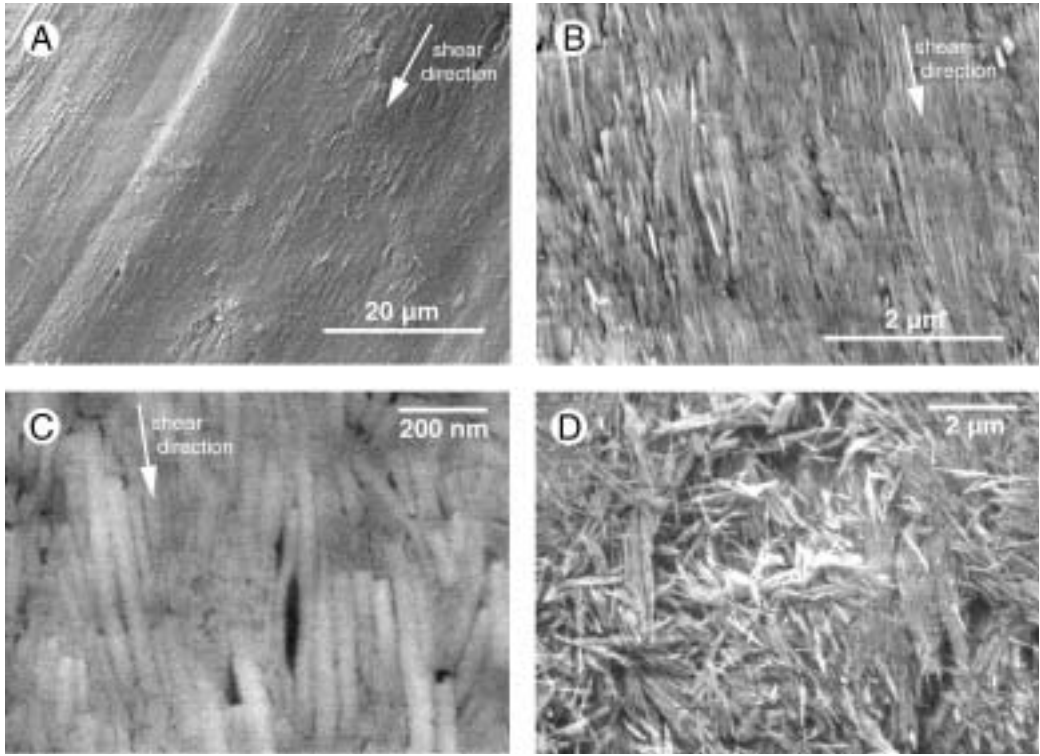
MOORE ET AL.

Fɪɢ. 5. Gouge textures; all are backscattered electron SEM images. A. General view (1800×) of boundary-shear surface (194°C, 70 MPa $\overline{\sigma}_n$ experiment). Shear surfaces are smooth and shiny, with corrugations or slickensides. The arrow indicates the direction of motion of the surface in the photo relative to the opposite shear surface. B. At 20,000×, the strong preferred alignment of the chrysotile fibers parallel to the direction of shear is visible (194°C, 70 MPa $\overline{\sigma}_n$ experiment). C. At 100,000×, the blunted ends of the fibers can be seen. The average fiber length of the experimental samples is shorter than that of the starting material (97°C, 150 MPa $\overline{\sigma}_n$ experiment). D. Gouge that is not directly on the shear surface has a more randomly oriented and more porous texture than that lining the shears; 10,000× (281°C, 70 MPa $\overline{\sigma}_n$ experiment).

Discussion

Combined data sets for chrysotile and their interpretation

Figure 6A combines the friction data from Figures 3 and 4 with those reported previously for chrysotile by Moore et al. (1996b, 1997). The values of μ from both data sets were measured at 3 mm displacement, in order to include the velocity step at 0.01 μm/s for the experiments in Figure 3. This was considered important, because of the time-dependent increases in strength at low velocities observed in several experiments. Only those heated experiments from the previous study that included a velocity step at 0.01 μm/s were included in Figure 6A. The experiments in Figure 4 were extrapolated to 3

mm displacement, and adjustments were made, where necessary, to make all of the data reflect an axial displacement rate of 0.1 μm/s. This plot illustrates the marked difference in strength between dry and water-saturated chrysotile at the same temperature and effective normal stress. Dry chrysotile is expected to be equally strong at other combinations of temperature and normal stress, and the shaded area represents the estimated range of dry values.

The room-temperature and heated strengths of water-saturated chrysotile follow different trends. The room-temperature data are well fit by a linear equation, with μ increasing by about 0.01 per 17 MPa increase in $\overline{\sigma}_n$. In contrast, all of the heated data were fit at least slightly better by logarithmic equations than by linear equations. The coefficient
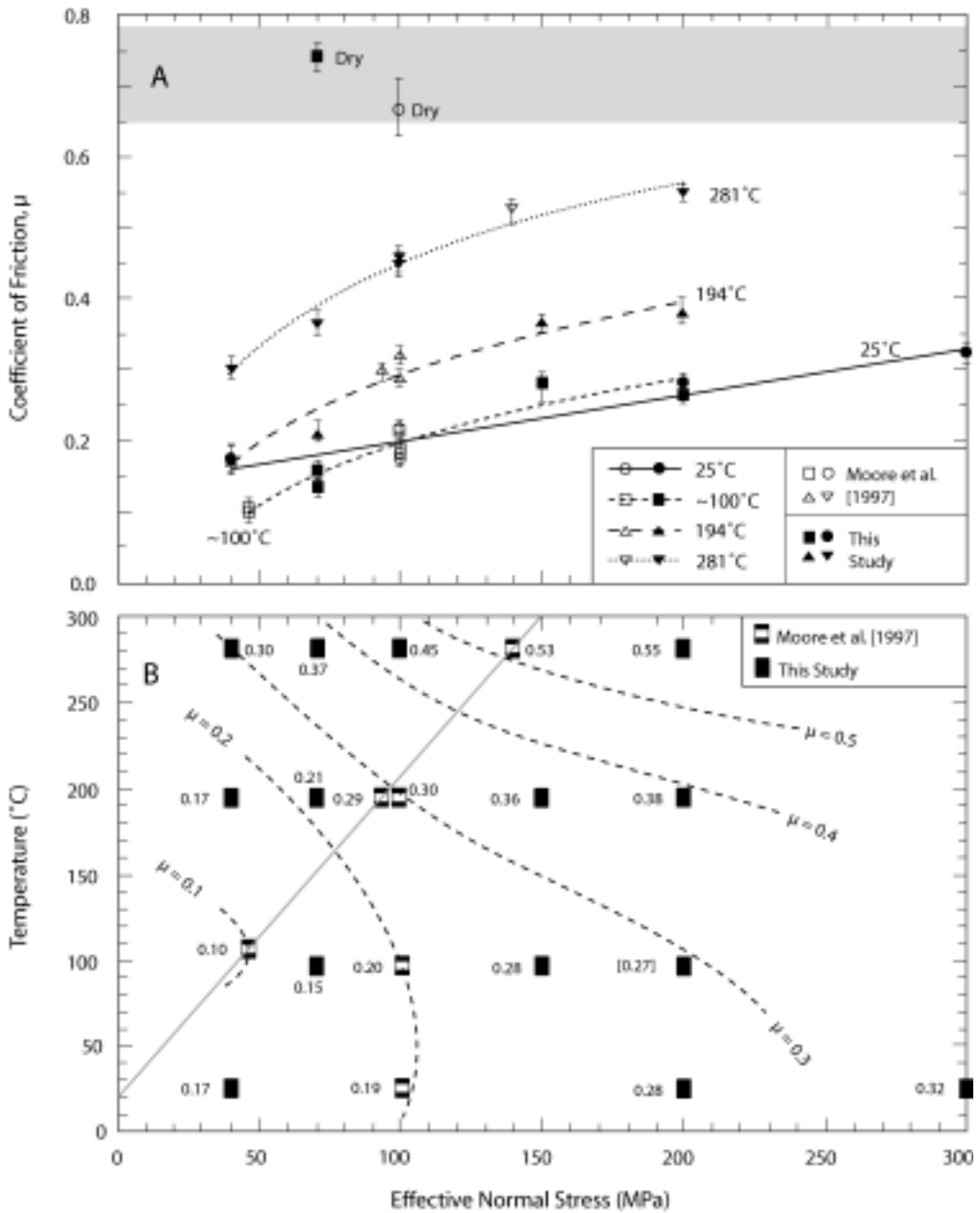
FIG. 6. Summary of frictional data for chrysotile gouge from this study and Moore et al. (1997), with one additional room-temperature data point at 300 MPa (Moore and Lockner, unpubl. data). A. Variation of μ with respect to $\overline{\sigma}_n$ at different temperatures. The ~100°C data comprise experiments at 97° and 107°C. Room-temperature data were fit with a linear equation, and those at elevated temperatures were fit with logarithmic equations. Strengths are interpolated to 3 mm axial displacement and 0.1 μm/s axial velocity (see text). B. Contour map of the variation in μ relative to temperature and $\overline{\sigma}_n$ for water-saturated chrysotile gouge using the data from Figure 6A and averaging multiple data points at the same conditions. The number in brackets is low compared to nearby data points. The solid grey line represents a hydrostatic pore-pressure gradient for a serpentine-filled San Andreas fault (see text).

of friction increases with increasing effective normal stress at all temperatures, but the overall rate of increase is greater for the heated samples. At a given temperature, the rate of increase of μ for the heated samples may be greater below 100 MPa $\overline{\sigma}_n$ than above. Temperature-induced increases in μ begin above 100°C, and the rate of change increases with increasing temperature. The combined temperature-stress effects cause the ~100°C trend to coincide with the room-temperature curve above 100 MPa but to drop below it at lower stresses. The 281°C trends approach the dry values at high effective stresses.

We previously attributed (Moore et al., 1997) the large difference between dry and water-saturated chrysotile strength to the tendency for the chrysotile fibers to take up adsorbed water (Young and Healey, 1954; Pundsack, 1956). In general, fine-grained and fibrous materials readily adsorb water because of their large specific surface areas (e.g., Faust and Fahey, 1962), and the hydrophilic character of chrysotile (Hodgson, 1966), mentioned previously, enhances this property. The adsorbed-water layer on chrysotile may act as a lubricant, facilitating the movement of chrysotile fibers past each other during shearing. Overall, compaction and heating (above 100°C) of chrysotile gouge gradually drives much of this water off the crystal surfaces, leading to an unusually strong pressure- and temperature-dependence of μ for chrysotile.

Our recent work (Moore and Lockner, 2004) has demonstrated that the type of behavior we proposed for chrysotile is applicable to phyllosilicates in general. Water in saturated phyllosilicate gouges forms thin, structured films between the plates, and the water in the films is bonded to the plate surfaces in proportion to the (001) surface energy of the mineral. Because of the strong preferred orientation of the (001) surfaces parallel to the shear planes, shear becomes concentrated in the water films, and the coefficient of friction reflects the stresses necessary to shear through them (Moore and Lockner, 2004).

Our work (Moore and Lockner, 2004) further suggests that, among other factors, the frictional strength of a layer-structured mineral is a function of the nature of the (001) surfaces—that is, whether the (001) crystal surfaces are all tetrahedral sheets (2:1 sheet silicates), all octahedral sheets (the hydroxide minerals brucite and gibbsite), or half tetrahedral and half octahedral sheets (1:1 sheet silicates). This presumably occurs because water molecules bond differently to the tetrahedral and octahedral surfaces (e.g., Kalinichev et al., 2002), and it may explain in part the differences in strength among the serpentine-mineral varieties. The octahedral sheet is always at the surface of the chrysotile fibers, whereas in lizardite, for example, the octahedral sheet is at one (001) surface of the crystal and the tetrahedral sheet is at the other. The tubular shape of chrysotile must also contribute to the difference in strength, but the exact mechanism is unknown.

The data for the water-saturated samples from Figure 6A are recast in a temperature-effective normal stress grid in Figure 6B, with contour lines of constant μ sketched in at intervals of 0.1. In this figure, the low-stress behavior of chrysotile is resolved as a minimum at ~100°C, defined by the $\mu = 0.1$ contour. From this minimum, μ rises to a maximum of ≥ 0.55 at the upper right-hand corner, at the maximum temperature-stress conditions. Other than for smectite clays such as montmorillonite, which have a similarly large contrast between dry and water-saturated strength (Morrow et al., 2000), these data for chrysotile may represent the widest possible variation in μ for a mineral at crustal pressure and temperature conditions.

The diagonal line in Figure 6B connects the experiments conducted by Moore et al. (1997) at conditions simulating burial depths of 3, 6, and 9 km in a serpentinite-filled San Andreas fault zone, for a hydrostatic fluid-pressure gradient. Conditions at depth were calculated assuming a surface temperature of 20°C, a geothermal gradient of ~30°/km (Lachenbruch and Sass, 1973), a serpentinite density of 2.55 gm/cm³ (Deer et al., 1962; Coleman, 1971), and a normal stress equal to the lithostatic pressure at all depths. With respect to the latter assumption, Mount and Suppe (1987) and Zoback et al. (1987) have shown that over most of its length, the maximum principal stress on the San Andreas fault is almost normal to the fault, making the normal stress approximately equal to the maximum stress. In-situ stresses near the San Andreas fault have been measured at a few places, principally in southern California (e.g., McGarr et al., 1982; Hickman et al., 1988; Stock and Healy, 1988; Zoback and Healy, 1992). The deepest measurements—to 3.5 km—were reported by Zoback and Healy (1992), who found that the maximum horizontal stress is approximately equal to or slightly greater than the vertical (lithostatic) stress, and it increases with depth at a rate similar to that of the vertical stress. Thus, the normal stress can be considered to

approximate the lithostatic stress, although stress conditions will certainly vary somewhat along the length of the fault. Temperature-stress profiles will also differ on other serpentinite-bearing faults. This line passes through the minimum and near the maximum values of μ in Figure 6B. Fluid pressures above hydrostatic levels would rotate this depth line to the left. A suprahydrostatic depth profile would still pass through a minimum at about 3 km depth, but the peak strength at deeper levels would be lower.

The velocity data from Table 2 are combined with those reported by Moore et al. (1997) in Figure 7. As mentioned previously, several of the higher-temperature strength plots in Figures 3 and 4 show a trend of increasing μ with displacement and time; much of the uncertainty in determinations of $\Delta_{ss}/\Delta\ln V$ arises from difficulties in separating the velocity-dependent, time-dependent, and strain-hardening effects. The error estimates included in Figure 7 represent an attempt to account for these uncertainties.

The rate dependence of chrysotile gouge strength is a complex function of temperature, sliding rate, and to some extent $\overline{\sigma}_n$ (Fig. 7). Overall, chrysotile shows velocity-strengthening behavior (μ increases with increasing velocity) at all the velocities tested at ~100°C; however, the two data points for the oven-dried sample, which showed stick-slip motion (Fig. 3A), are velocity weakening (μ decreases with increasing velocity). Nearly all the 281°C results are velocity weakening. Both velocity-strengthening and velocity-weakening behavior are observed at room-temperature and 194°C, but their trends with respect to velocity are reversed. The data points from the 200 MPa experiments tend to be shifted to lower values compared to the other results.

Reinen et al. (1994) presented a two-stage model to explain the velocity dependence of serpentine minerals at room temperature. Determining the applicability of their model to the velocity behavior of chrysotile at elevated temperatures is beyond the scope of this investigation. We note that the trends in Figure 7 show an interesting correlation with Figure 6B in that the typically velocity-strengthening ~100°C results are associated with the low-strength minimum and the largely velocity-weakening 281°C results with the maximum. Mixed velocity behavior is characteristic of the areas in between. In the same way, the ~100°C trends in Figure 6A may in part reflect the largely velocity-strengthening behavior of chrysotile at that temperature, with the most positive

values of $\Delta\mu_{ss}/\Delta\ln V$ measured at the lowest effective normal stresses.

Application to fault zones

The chrysotile content of serpentinite has been shown to increase with increasing amounts of shearing (Page, 1968; Coleman and Keith, 1971; Mumpton and Thompson, 1975; O'Hanley, 1991), and as a result chrysotile-lined principal slip surfaces potentially could control the behavior of a serpentinite-filled fault. The presence of serpentinite has commonly been invoked to explain the occurrence of creep in the San Andreas fault system (e.g., Irwin and Barnes, 1975). The depth profile in Figure 6B predicts a weak, stably sliding fault at shallow depths and a stronger, potentially seismic fault at the deepest levels. The velocity data in Figure 7 suggest the occurrence of mixed behavior at intermediate depths of about 5–8 km, as potentially unstable, velocity-weakening conditions are reached at shallower depths for velocities <0.1 μm/s than for velocities >0.1 μm/s. The slowest axial velocity included in Figure 7, 0.001 μm/s, corresponds to a slip rate along the sawcut surface of 36.4 mm/yr, whch is on the order of average slip rates in the San Andreas system. Instabilities could potentially be initiated in this intermediate depth interval.

The changing character of a chrysotile-lined fault zone with increasing depth, outlined above, may be consistent with the pattern of aseismic creep of the Hayward fault, located east of San Francisco Bay in northern California. The Hayward fault is characterized by aseismic creep at the surface, but it has also produced large-magnitude earthquakes (e.g., Simpson, 2000). Although there is some question about the depth extent of creep at the northern and southern ends of the Hayward fault (e.g., Bürgmann et al., 2000; Simpson et al., 2001), much of the fault may be locked at depths greater than about 5 km in the seismogenic zone (Savage and Lisowski, 1993; Simpson et al., 2001; Waldhauser and Ellsworth, 2002). Chrysotile-rich fault gouge has been collected from a trench crossing a strand of the Hayward fault (D. St. Hayward sample, analyzed by Moore et al., 1996a) and from other surface exposures along the fault.

Concluding Remarks

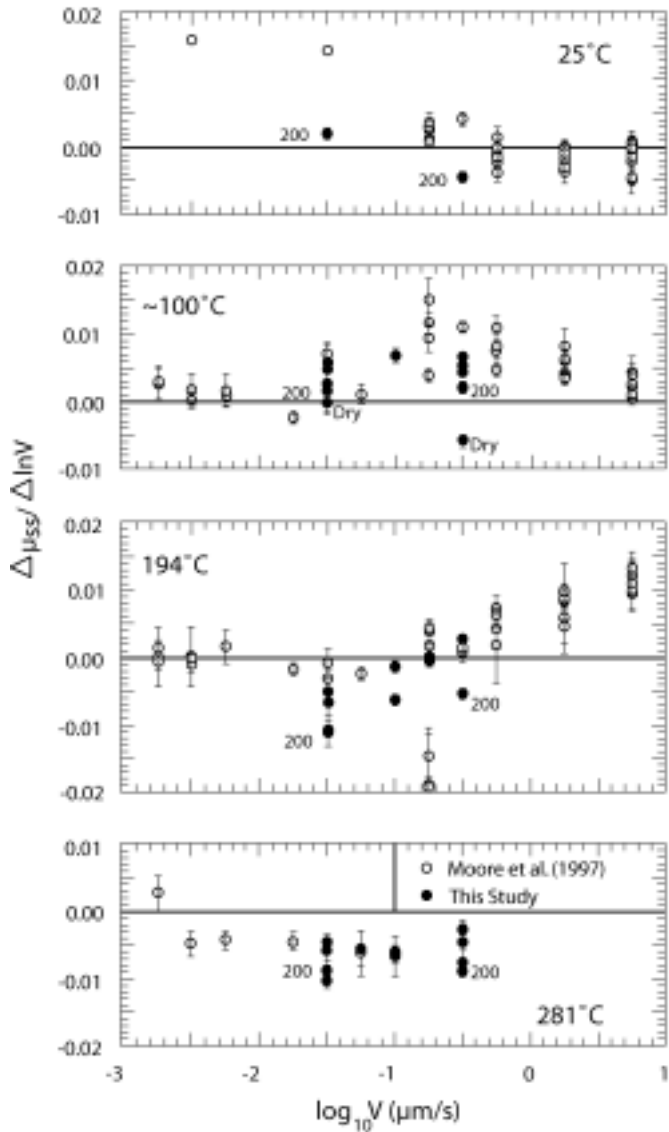The serpentine mineral chrysotile displays an unusual strength profile within a fault zone, caused

FIG. 7. Steady-state velocity dependence of μ at 25°, ≈100°, 194°, and 281°C, combining the velocity data in Table 2 with those plotted in Figures 10 and 11 of Moore et al. (1997, p. 14,797). The horizontal axis is the log of velocity, and the data are plotted at the mid-point of the velocity step.

by its strong water-sorptive properties. The coefficient of friction goes through a minimum of μ = 0.1 at about 3 km depth, and slip should be stable at this level. At greater depths, not only does chrysotile become significantly stronger (three- to fivefold increase in μ by 9 km) but it also is likely to slip unstably (seismically). The details of chrysotile frictional behavior within a fault would not have been predicted from the room-temperature data. Although chrysotile probably represents an extreme case, these results nevertheless illustrate the potential hazards of extrapolating room-temperature friction data to predict fault-zone behavior at depth. The presence of chrysotile-lined shear surfaces may possibly explain the seismicity patterns of the Hayward fault of northern California, which creeps

aseismically at shallow depths but which may be locked at depths greater than about 5 km over much of its length.

Acknowledgments

REFERENCES

Bürgmann, R., Schmidt, D., Nadeau, R. M., d'Alessio, M., Fielding, E., Manaker, D., McEvilly, T. V., and Murray, M. H., 2000, Earthquake potential along the northern Hayward fault, California: Science, v. 289, p. 1178–1182.

Coleman, R. G., 1971, Petrologic and geophysical nature of serpentinites: Geological Society of America Bulletin, v. 82, p. 897–918.

Coleman, R. G., and Keith, T. E., 1971, A chemical study of serpentinization—Burro Mountain, California: Journal of Petrology, v. 12, p. 311–328.

Deer, W. A., Howie, R. A., and Zussman, J., 1962, Rock-forming minerals, v. 3. Sheet silicates: New York, NY, John Wiley and Sons, p. 170–190.

Faust, G. T., and Fahey, J. J., 1962, The serpentine group minerals: U. S. Geological Survey Professional Paper 384-A, 91 p.

Hickman, S. H., Zoback, M. D., and Healy, J. H., 1988, Continuation of a deep borehole stress measurement profile near the San Andreas fault. 1. Hydraulic fracturing stress measurements at Hi Vista, Mojave Desert, California: Journal of Geophysical Research, v. 93, p. 15,183–15,195.

Hodgson, A. A., 1966, Fibrous silicates: London, UK, Royal Institute of Chemistry, 46 p.

Irwin, W. P., and Barnes, I., 1975, Effect of geologic structure and metamorphic fluids on seismic behavior of the San Andreas fault system in central and northern California: Geology, v. 3, p. 713–716.

Kalinichev, A. G., Cygan, R. T., Wang, J., and Kirkpatrick, R. J., 2002, Structure and dynamics of mineral/water interfaces: Molecular dynamics simulations of clays and clay-related phases [abs.]: EOS (Transactions, American Geophysical Union), v. 83, Fall Meeting Supplement, p. F1396.

Lachenbruch, A. H., and Sass, J. H., 1973, Thermomechanical aspects of the San Andreas fault system, *in* Kovach, R. L., and Nur, A., eds., Proceedings of the Conference on the Tectonic Problems of the San Andreas Fault System: Stanford University Publications in the Geological Sciences, v. 13, p. 192–205.

Logan, J. M., and Rauenzahn, K. A., 1987, Frictional dependence of gouge mixtures of quartz and montmorillonite on velocity, composition, and fabric: Tectonophysics, v. 144, p. 87–108.

McGarr, A., Zoback, M. D., and Hanks, T. C., 1982, Implications of an elastic analysis of in situ stress measurements near the San Andreas fault: Journal of Geophysical Research, v. 87, p. 7797–7806.

Moore, D. E., and Lockner, D. A., 2004, Crystallographic controls on the frictional behavior of dry and water-saturated sheet-structure minerals: Journal of Geophysical Research, in press.

Moore, D. E., Lockner, D. A., Summers, R., Byerlee, J. D., and Ma, S., 1996a, Sample characterization and strength measurements of serpentinite gouges: U.S. Geological Survey Open-File Report 96–702, 88 p.

Moore, D. E., Lockner, D. A., Ma, S., Summers, R., and Byerlee, J. D., 1997, Strengths of serpentinite gouges at elevated temperatures: Journal of Geophysical Research., v. 102, p. 14,787–14,801.

Moore, D. E., Lockner, D. A., Summers, R., Ma, S., and Byerlee, J. D., 1996b, Strength of chrysotile-serpentinite gouge under hydrothermal conditions: Can it explain a weak San Andreas fault?: Geology, v. 24, p. 1041–1044.

Morrow, C. A., Moore, D. E., and Lockner, D. A., 2000, The effect of mineral bond strength and adsorbed water on fault gouge frictional strength: Geophysical Research Letters, v. 27, p. 815–818.

Mount, V. S., and Suppe, J., 1987, State of stress near the San Andreas fault: Implications for wrench tectonics: Geology, v. 15, p. 1143–1146.

Mumpton, F. A., and Thompson, C. S., 1975, Mineralogy and origin of the Coalinga asbestos deposit: Clays and Clay Minerals, v. 23, p. 131–143.

O'Hanley, D. S., 1991, Fault-related phenomena associated with hydration and serpentine recrystallization during serpentinization: Canadian Mineralogist, v. 29, p. 21–35.

O'Hanley, D. S., Chernosky, J. V., Jr., and Wicks, F. J., 1989, The stability of lizardite and chrysotile: Canadian Mineralogist, v. 27, p. 483–493.

Page, N. J., 1968, Serpentinization in a sheared serpentinite lens, Tiburon Peninsula, California: U. S. Geological Survey Professional Paper 600-B, p. B21–B28.

Pundsack, F. L., 1956, The properties of asbestos. II. The density and structure of chrysotile: Journal of Physical Chemistry, v. 60, p. 361–364.

Reinen, L. A., and Tullis, T. E., 1995, Microstructural evidence of strain localization and distributed strain in serpentine friction experiments [abs.]: EOS (Transactions, American Geophysical Union), v. 76, Fall Meeting Supplement, p. F560.

Reinen, L. A., Weeks, J. D., and Tullis, T. E., 1994, The frictional behavior of lizardite and antigorite serpentinites: Experiments, constitutive models, and implications for natural faults: Pure and Applied Geophysics, v. 143, p. 317–358.

Rice, J. R., and Gu, J., 1983, Earthquake aftereffects and triggered seismic phenomena: Pure and Applied Geophysics, v. 121, p. 187–219.

Savage, J. C., and Lisowski, M., 1993, Inferred depth of creep on the Hayward fault, central California: Journal of Geophysical Research, v. 98, p. 787–793.

Simpson, R. W., 2000, Watching the Hayward Fault: Science, v. 289, p. 1147–1148.

Simpson, R. W., Lienkaemper, J. J., and Galehouse, J. S., 2001, Variations in creep rate along the Hayward Fault, California, interpreted as changes in depth of creep: Geophysical Research Letters, v. 28, p. 2269–2272.

Stock, J. M., and Healy, J. H., 1988, Continuation of a deep borehole stress measurement profile near the San Andreas fault. 2. Hydraulic fracturing stress measurements at Black Butte, Mojave Desert, California: Journal of Geophysical Research, v. 93, p. 15,196–15,206.

Waldhauser, F., and Ellsworth, W. L., 2002, Fault structure and mechanics of the Hayward Fault, California, from double-difference earthquake locations: Journal of Geophysical Research, v. 107 [doi:10.1029/2000JB000084, ESE 3,15 p.].

Young, G. J., and Healey, F. H., 1954, The physical structure of asbestos: Journal of Physical Chemistry, v. 58, p. 881–884.

Zhang, S., Tullis, T. E., and Scruggs, V. J., 2001, Implications of permeability and its anisotropy in a mica gouge for pore pressures in fault zones, in Boland, J., and Ord, A., eds., Deformation processes in the Earth's crust: Tectonophysics, v. 335, p. 37–50.

Zoback, M. D., and Healy, J. H., 1992, In situ stress measurements to 3.5 km depth in the Cajon Pass scientific research borehole: Implications for the mechanics of crustal faulting: Journal of Geophysical Research, v. 97, p. 5039–5052.

Zoback, M. D., Zoback, M. L., Mount, V. S., Suppe, J., Eaton, J. P., Healy, J. H., Oppenheimer, D., Reasenberg, P., Jones, L., Raleigh, C. B., Wong, I. G., Scotti, O., and Wentworth, C., 1987, New evidence on the state of stress of the San Andreas fault system: Science, v. 238, p. 1105–1111.